Chapter 6

Effect of electropulsing on stability of retained austenite and nanostructured bainite

6.1. Introduction

The electropulsing technique has been known to accelerate recrystallization and phase transformation kinetics [49,229]. It plays a significant role in phase transformation by enhancing diffusion through the drift of atoms [143]. There is a possibility that electropulsing can increase the diffusivity of carbon, which is essential during the nucleation stage of bainite. Nanostructured bainite formed after austempering at 250 °C for 48 hours contains a considerable amount of retained austenite. To investigate the stability of austenite and bainite, as well as to observe any possible transformation from fresh austenite to bainite, the material is subjected to a high-density electric current pulse for one time and repeatedly for five times. The aim is to assess the effect of EP on the microstructure and phase transformation behaviour of the steel.

6.2. Results

The nanostructured bainitic steel austempered for 48 hours (D2-48h) was subjected to electropulsing treatment at ambient temperature. The parameters of the EP are provided in Table 2.2 of the experimental section, and the resulting waveform is illustrated in Figure 6.1a. Two categories of samples are choosen in this experiment. The first category receives a single pulse (D2-48h-EP-1) and is repeated five times (D2-48h-EP-5) at a high current density (8.8 kA/mm^2). The second category undergoes a single pulse (D2-48h-EP-1-LCD) at a relatively low current density (6.3 kA/mm^2) to minimize thermal effects.

The temperature rise in the high current density sample is calculated using Equation 3.1 considering specific heat capacity (C_p) as 500 J/kg K, time period (Δt) as 65.7 µs, peak current density (I) as 8.8 kA/mm^2, density of the material (d_m) as 7.53 gm/cm^3 and resistivity (ρ_r) as 9.2 x 10^{-7}Ωm, which was measured by four-probe technique. The calculated instantaneous temperature rise is approximately 1200 °C. On the other hand, for the samples treated with low

current density (6.3 kA/mm^2), the time period is shorter, specifically 52 µs. The corresponding temperature rise is calculated to be approximately 470 °C. The temperature rise in this case is high compared to ECAPed material because of higher resistivity and duration (65 µs) of electropulsing.

To validate the high temperature-rise in the D2-48h-EP-1 and D2-48h-EP-5 samples, real-time colour changes of the samples (Figure 6.1b) during the electropulsing process are compared with data previously reported in steel research [230]. The comparison confirms the substantial increase in temperature during electropulsing.

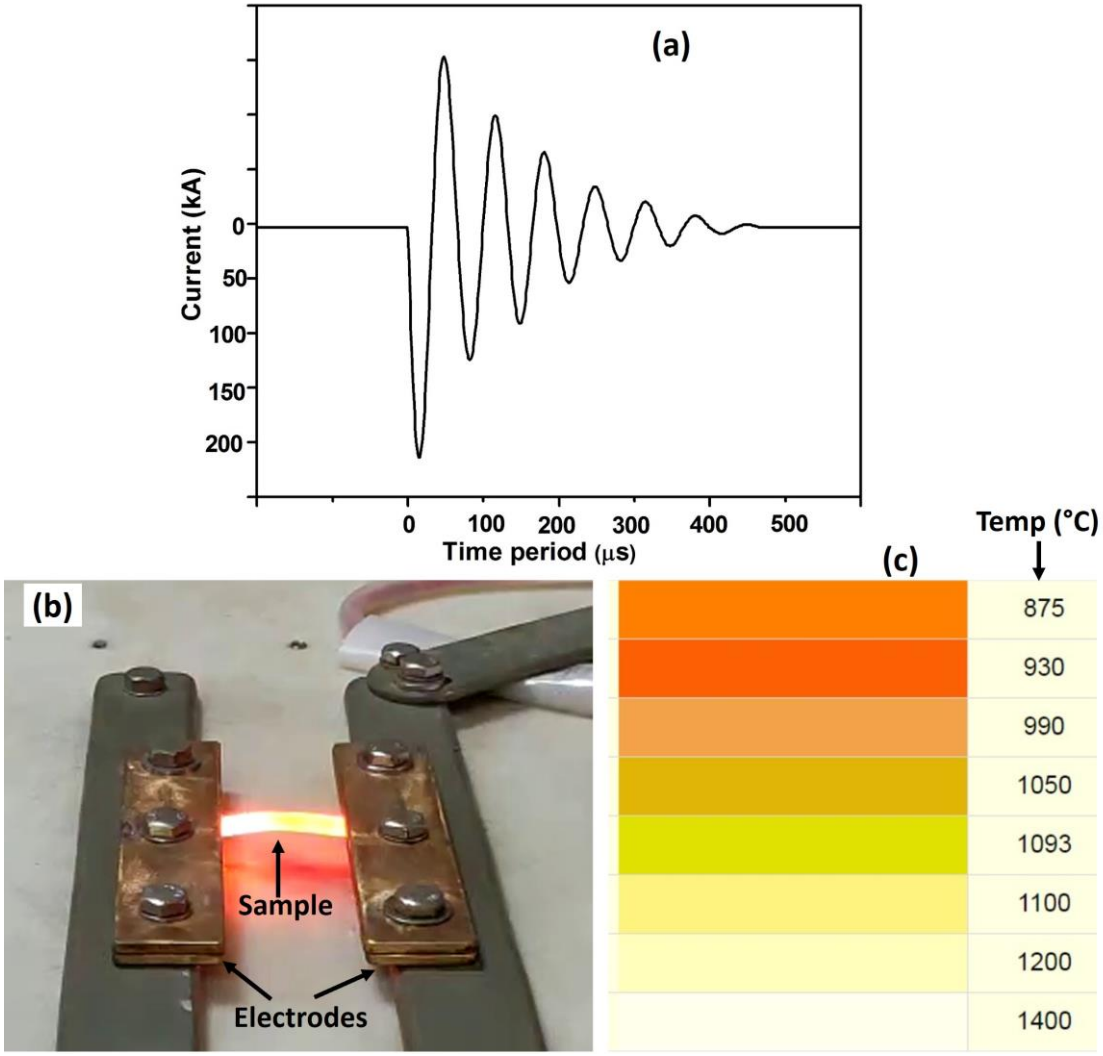

Figure 6.1. *(a) Wave form of electropulsing of D2-48h sample, (b) Realtime image of the sample during electropulsing treatment and (c) Colour of the steel at different temperatures (°C)* [230].

The SEM secondary electron micrograph of the D2-48h sample displays the coexistence of retained austenite (flat uncorroded regions) and nanostructured bainite (corroded regions) (Figure 6.2a). The EBSD phase map estimates the volume percent of bainite and retained austenite (RA) to be 59% and 41%, respectively (Figure 6.2c). Upon subjecting the D2-48h sample to a single pass of electropulsing (D2-48h-EP-1), fine carbides (small particles) precipitate as observed in the SEM micrograph (Figure 6.2b). The volume percent of retained austenite is reduced to 19%, while the bainite content increases approximately to 81%, as evidenced by the EBSD phase map in Figure 6.2d. With repeated pulsing five times (Figure 6.2g), the volume percent of retained austenite is marginally reduced to 14%. The fine carbides present or precipitated during the initial pulses get dissolved due to repeated exposure to electropulsing (Figure 6.2e). Since the EBSD scanning cannot fully resolve fine nano-sized carbides, the estimated quantity of bainitic ferrite is approximate. However, it is evident that retained austenite is decomposing into other phases.

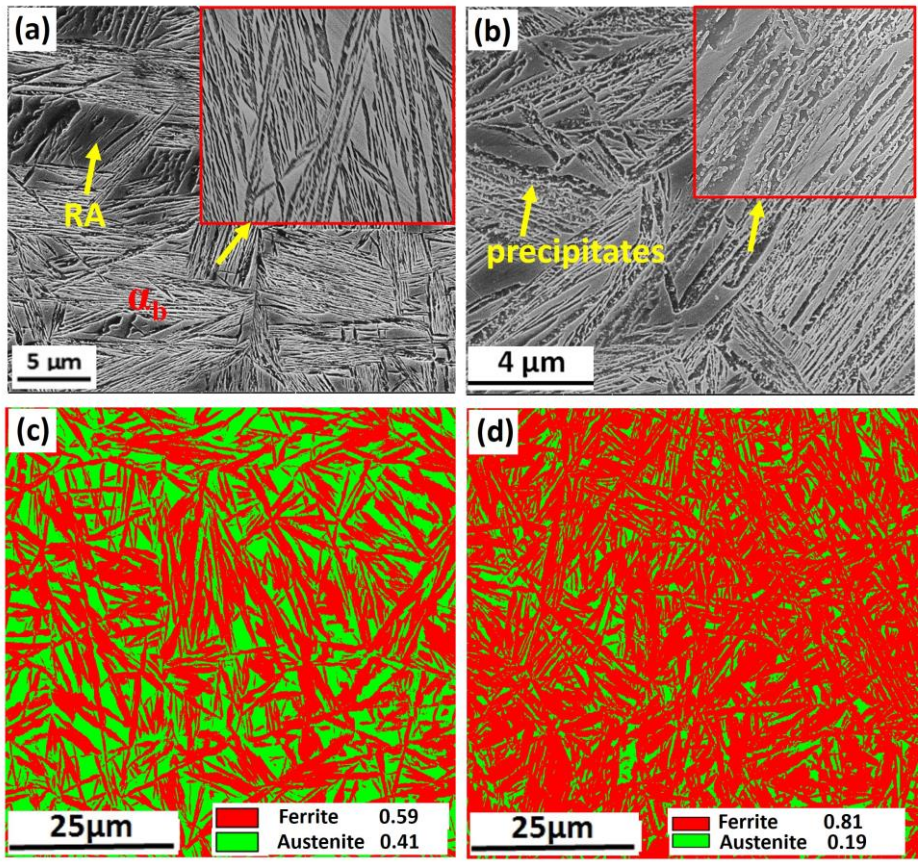

Figure 6.2. *SEM secondary electron micrographs of (a) D2-48h, (b) D2-48h-EP-1, and EBSD phase maps of (c) D2-48h, (d) D2-48h-EP-1 (Symbol α_b denotes bainite and RA is retained austenite, and FRA is filmy retained austenite).*

In contrast, the low current density sample (D2-48h-EP-1-LCD) does not show significant carbides (Figure 6.2f), but the phase map (Figure 6.2h) indicates a higher amount of bainitic ferrite, approximately 68%, compared to the D2-48h sample. Nevertheless, the bainitic ferrite content is lower than that observed in the high current density pulsing.

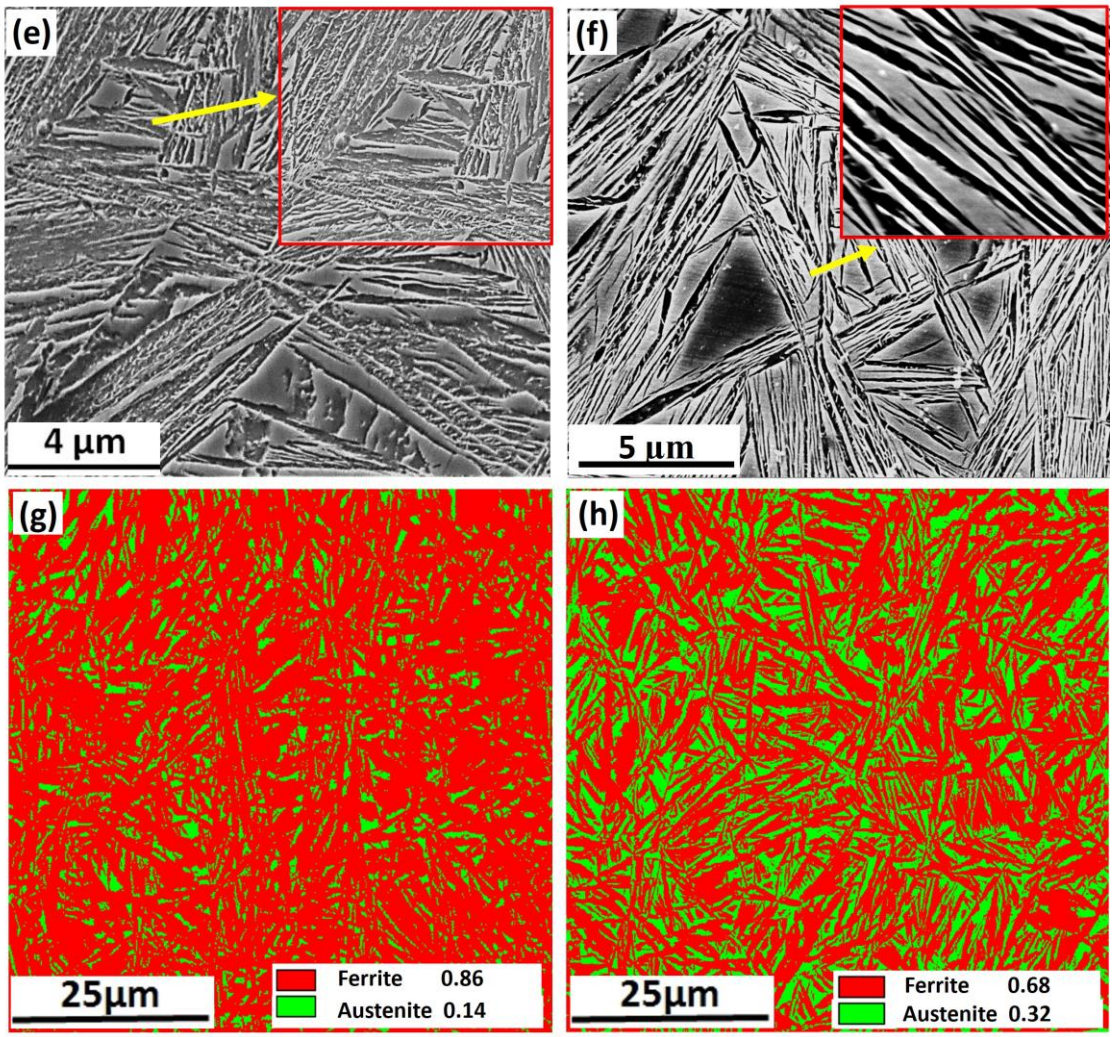

Figure 6.2 (continue…) *SEM secondary electron micrographs of (e) D2-48h-EP-5, (f) D2-48h-EP-1-LCD and EBSD phase maps of (g) D2-48h-EP-5, (h) D2-48h-EP-1-LCD.*

The XRD patterns of the D2-48h sample indicate the presence of only two phases, bainite and retained austenite (RA), in the alloy (Figure 6.3a). Using Rietveld refinement, the volume percent of these phases are determined to be 55% for bainite and 45%

for austenite, respectively. Following one pulse (D2-48h-EP-1), the intensity of the retained austenite peak decreases, while that of bainite increases (Figure 6.3a). This suggests that the retained austenite phase decomposes into other phases like bainite, martensite, ferrite, or carbide. However, due to overlapping peaks at the same 2θ position, determining the phase fractions accurately through Rietveld refinement becomes challenging, particularly when intense peaks of multiple phases coincide. Additionally, carbide peaks often merge into the background due to their smaller volume fraction and close 2θ positions with significant peaks of bainite and austenite. The intensity of austenite peaks also decreases slightly after five pulses (D2-48h-EP-5). In the low current density sample (D2-48h-EP-1-LCD), the intensity of austenite decreases to a lesser extent compared to the high current density samples. This observation indicates that the conversion of austenite to bainite/martensite is related to the current density used in the electropulsing process. In other words, higher current densities seem to promote a more significant transformation of austenite to bainite or martensite, while lower current densities result in a relatively lower transformation process.

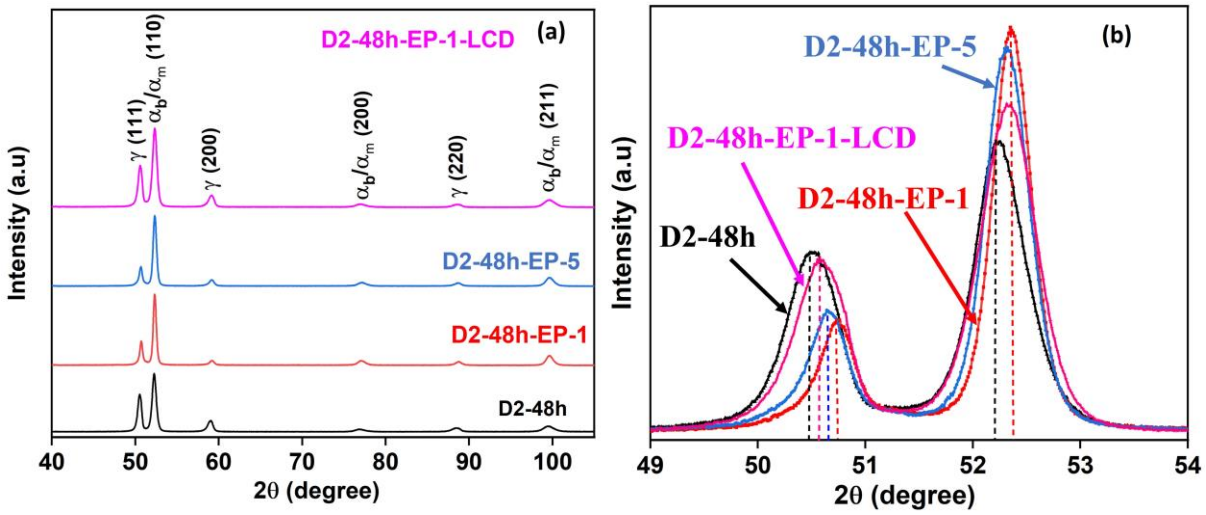

Figure 6.3. *XRD patterns of (a) D2-48h, D2-48h-EP-1, D2-48h-EP-5, D2-48h-EP-1-LCD and (b) magnified view of (111) and (110) peaks of austenite and bainite phases respectively.*

The (111) peaks of austenite and (110) bainite/martensite phases (Figure 6.3b) reveal peak shifting towards a higher angle side after one pulse (D2-48h-EP-1, D2-48h-EP-1-LCD)

of the D2-48h sample. In contrast, the peaks shift towards the lower angle side after five pulses (D2-48h-EP-5) compared to the D2-48h-EP-1 sample. The dislocation density of the D2-48h sample, calculated from the MWH plot, is $26\times10^{15}/m^2$ for bainite and $1.6\times10^{15}/m^2$ for austenite phases, respectively (Table 6.1). After one pulse (D2-48h-EP-1), the dislocation density of bainite increases to $39\times10^{15}/m^2$, and that of austenite is $3.6\times10^{15}/m^2$. The dislocation density of the D2-48h-EP-5 in the austenite phase is nearly the same as D2-48h-EP-1, but it decreases to $21\times10^{15}/m^2$ in the bainite phase. In the case of the lower current density sample, the dislocation density significantly increases compared to the initial D2-48h sample in both the bainite and retained austenite phases.

After one pulse of the D2-48h sample, the lattice parameter of retained austenite decreased, whereas after five pulses, it increased again. The carbon content in RA is also reduced from 1.15 mass % in D2-48h to 0.9 mass % in D2-48h-EP-1 due to precipitation of carbides. However, after five pulses, it increased to 1 mass % (Table 6.1). This indicates the dissolution of carbides in the matrix, which also results in shifting the austenite and bainite peaks towards lower 2θ values due to the increase in carbon content. The carbon content in the D2-48h-EP-1-LCD sample is not significantly decreased, as a lesser amount of carbide is precipitated compared to the high current density samples.

Table 6.1. XRD peak profile analysis

Sample		Dislocation density ($x10^{15}/m^2$)	Austenite lattice parameter (Å)	Carbon content in retained austenite (mass%)
D2-48h	Bainite	26	3.623	1.15
	Austenite	1.6		
D2-48h-EP-1	Bainite	39	3.612	0.9
	Austenite	3.6		
D2-48h-EP-5	Bainite	21	3.617	1
	Austenite	3.1		
D2-48h-EP-1-LCD	Bainite	42	3.620	1.07
	Austenite	4		

The TEM bright field image and corresponding diffraction pattern of the austempered sample (D2-48h) demonstrate the presence of bainite (appearing white) and retained austenite (appearing dark) (Figure 6.4a). Carbon clusters and carbides, around 15 nm in size, are also visible inside bainite plates, as indicated by the high magnification image. After one pulse of the austempered sample (D2-48h-EP-1), the bainitic sheaf size is found to be increased, showing fresh formation of bainite (Figure 6.4b). The BF image (Figure 6.4c) and dark field (DF) images (Figure 6.4d) of the D2-48h-EP-1 sample confirm the precipitation of carbides in both bainite and retained austenite. The carbides formed generally have an elongated shape with an average length of 53 ± 22 nm. In another BF image, a blocky retained austenite is depicted (Figure 6.4e), and its corresponding DP (Figure 6.4f) demonstrates the presence of the BCC phase. This indicates that part of the blocky austenite has transformed to either bainite or martensite.

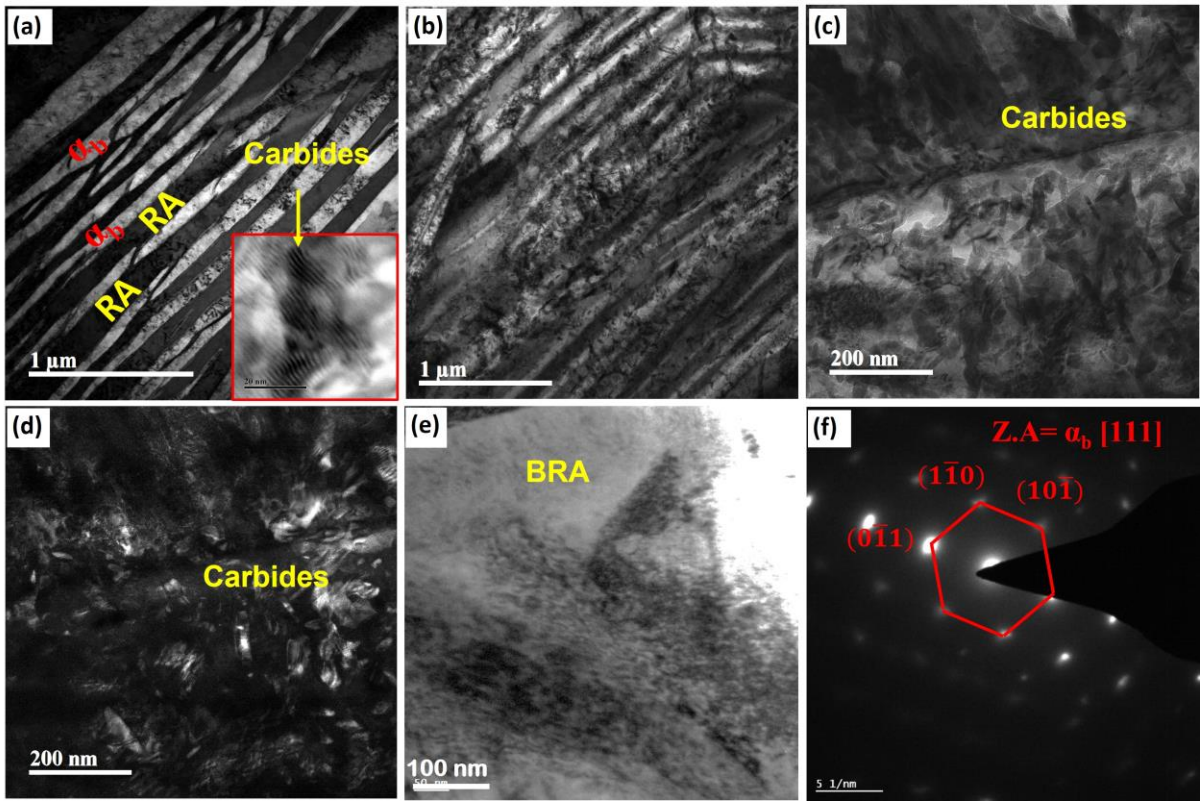

Figure 6.4. *TEM BF images of (a) D2-48h with a magnified region of bainite showing carbides, (b, c) D2-48h-EP-1 and (d) DF images of D2-48h-EP-1 sample. A blocky retained austenite region of D2-48h-EP-1 sample is shown in (e) and its corresponding DP in (f).*

In another region of RA, as shown in the TEM bright field image (Figure 6.5a), the presence of martensite with a twinned relationship is revealed. The DF images taken from the spots marked in the corresponding diffraction pattern (Figure 6.5b) are shown in Figure 6.5b and c. The DF images corresponding to spot 1 and 2 show the presence of fine precipitation of carbides and martensite plates.

A TEM bright field image of a sheaf containing FRA is shown in Figure 6.5d, and its magnified view is presented in Figure 6.5e. Some fine precipitates are also observed inside FRA, and the corresponding diffraction pattern (Figure 6.5f) indicates the formation of epsilon (ε) carbides within it.

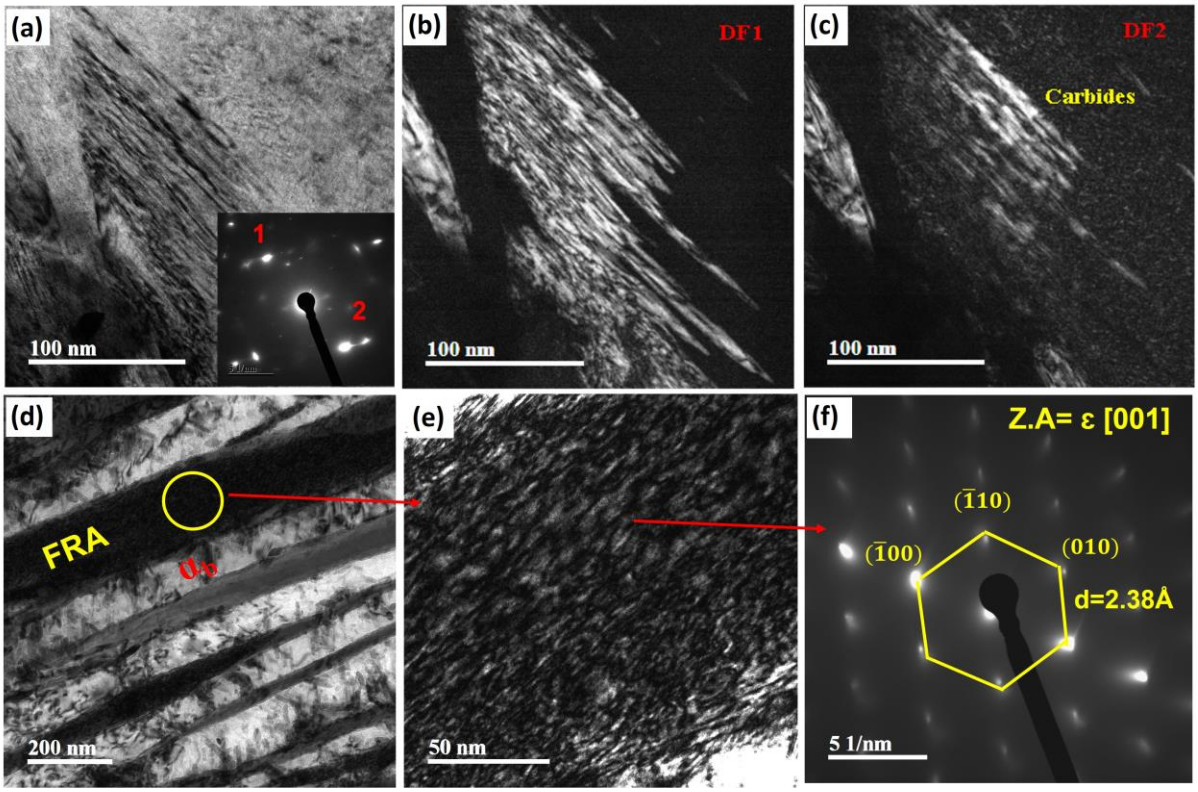

Figure 6.5. *TEM images of a BRA region of D2-48h-EP-1 sample (a) BF image and corresponding DP, DF from DP (b) spot 1 and (c) spot 3. (d) BF image showing FRA and its magnified region and corresponding DP in (e) and (f) respectively. (The spot size of beam is narrowed to 3 nm).*

After five pulses (D2-48h-EP-5) precipitates are partially dissolved in the bainite phase as shown in the TEM BF (Figure 6.6a) and DF images (Figure 6.6c). However, the precipitates are fully dissolved in the RA phase as shown by yellow arrow mark. In a region of BRA shown in Figure 6.6d, the lenticular feature with sharp boundaries is confirmed to be martensite.

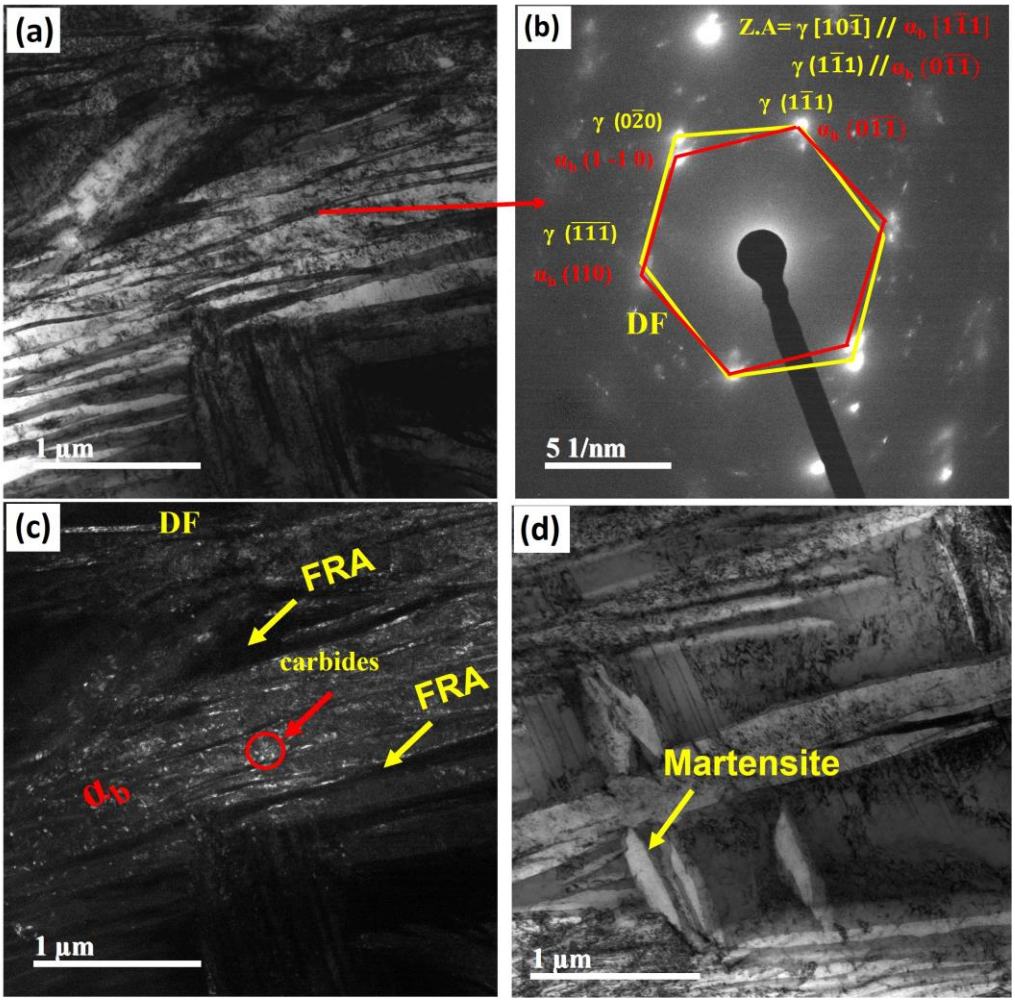

Figure 6.6. *TEM micrographs of D2-48h-EP-5 (a) BF (b) DP, (c) DF and (d) BF image showing martensite formation in BRA.*

The lower current density sample (D2-48h-EP-1-LCD) is also examined by TEM. The BF image (Figure 6.7a) shows the presence of carbides that are slightly larger than those in the austempered sample but smaller than those in the higher current density sample (D2-48h-EP-1). Additionally, new bainite plates are formed near the previously formed sheaf. The DP (Figure 6.7b) taken from the BF region corresponds to the [113] zone axis of bainite, which is

further confirmed by the simulation of the DP as shown in Figure 6.7d. The DF image corresponding to the spot shown in the DP confirms the presence of carbides in the bainite phase, but no carbides are observed in the RA phase.

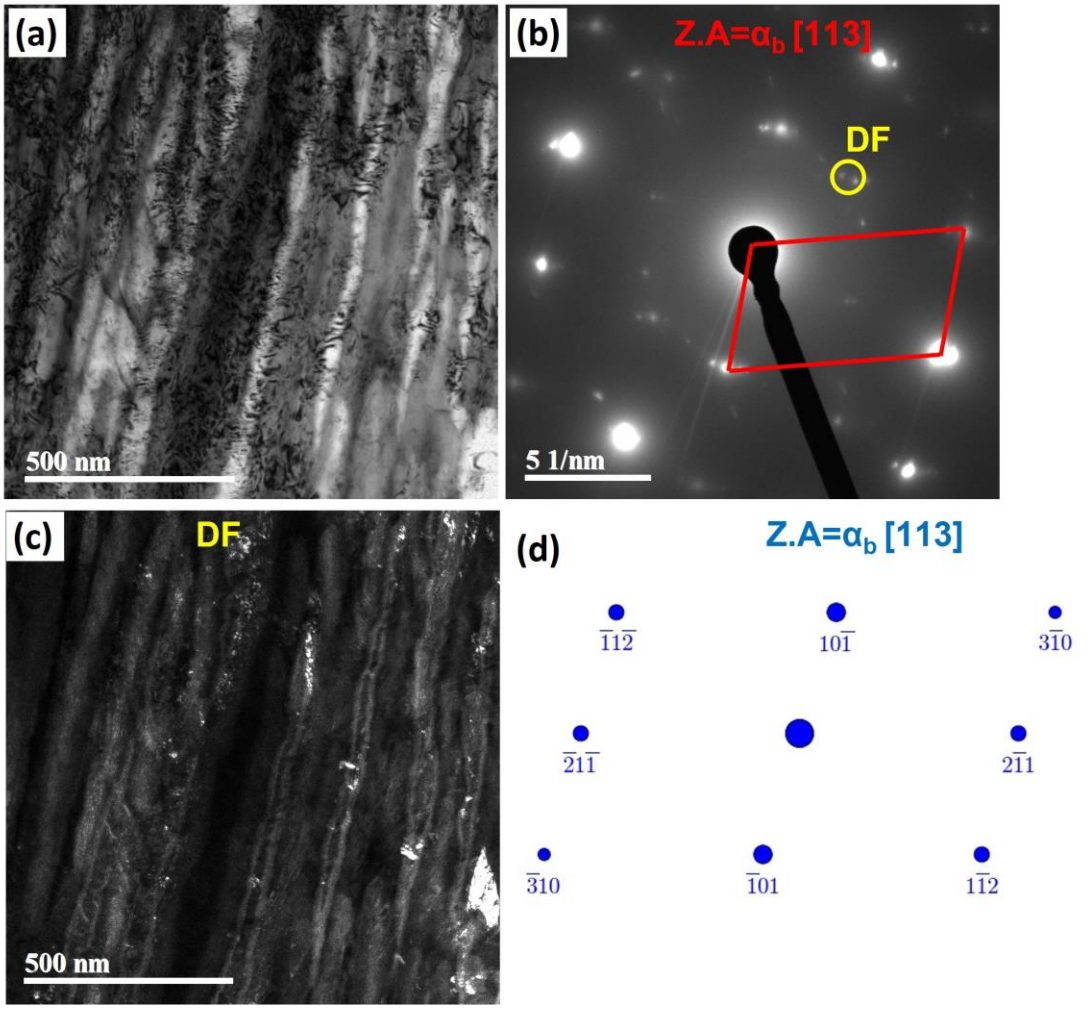

Figure 6.7. *TEM images of D2-48h-EP-1-LCD sample (a) BF, (b) DP and (c) DF from spot shown in DP in Figure b. (d) simulated diffraction pattern corresponding to α_b [113] zone axis.*

In a selected region of BRA in the D2-48h-EP-1-LCD sample, the application of pulse current results in the formation of martensite with twin orientation, as depicted in the TEM BF images in Figure 6.8a and Figure 6.8b. The corresponding diffraction pattern (Figure 6.8c and f) analysis reveals that the zone axis is [113]. Notably, the DF images of Figure 6.8d and exhibit the presence of twins and sharp boundaries within the martensite structure, respectively.

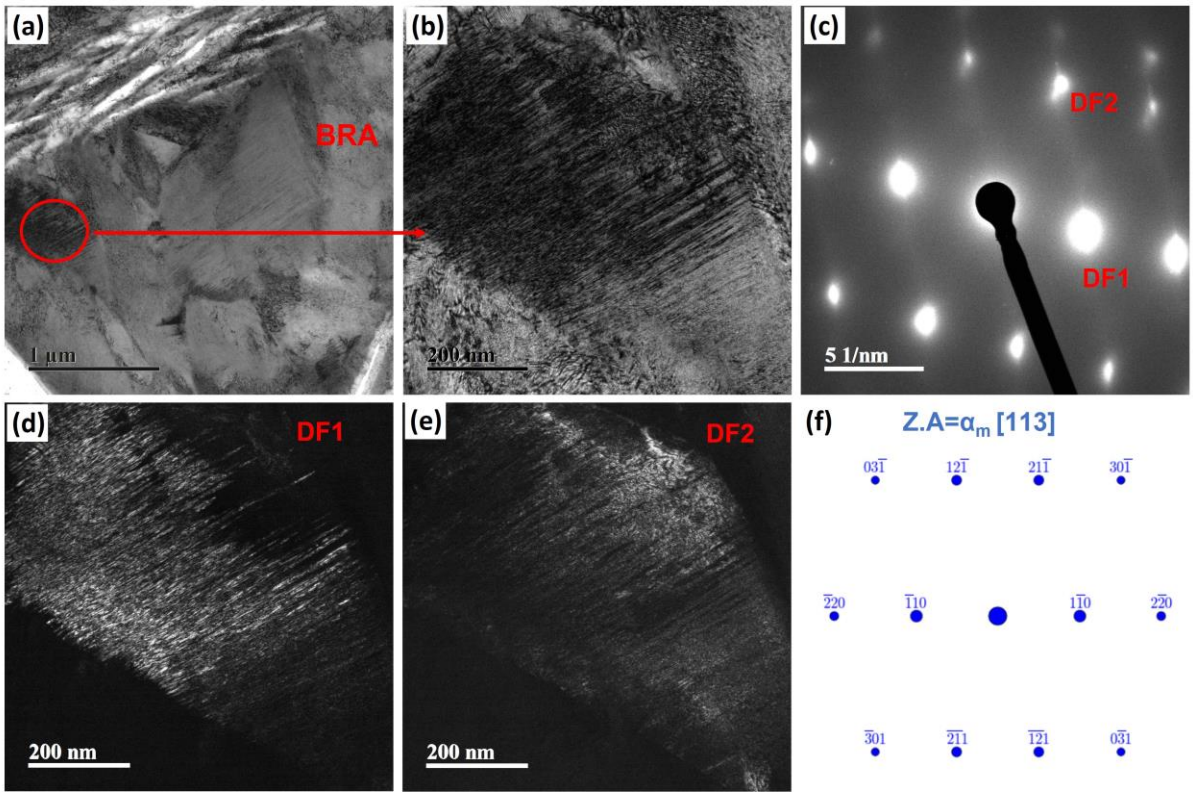

Figure 6.8. *TEM micrographs of D2-48h-EP-1-LCD from a BRA region (a) BF, (b) BF (magnified region of circled area in figure a), (c) DP, (d) DF1 and (e) DF2. (f) simulated diffraction pattern corresponding to α_m [113] zone axis.*

Utilizing the EBSD Kernel Average Misorientation (KAM) map with a 5° misorientation angle, strain analysis is performed. In the bainite phase of the D2-48h sample (Figure 6.9a), the average KAM value is about 1°. After one pulse treatment (D2-48h-EP-1), the average KAM value increases to 1.07° as shown in Figure 6.9b, indicating a slight increase in strain. However, with repeated pulsing (D2-48h-EP-5), the average KAM value decreases to 0.95°, indicating a decrease in strain, as shown in Figure 6.9e. Similarly, in the RA phase of the D2-48h sample (Figure 6.9c), the average KAM value is found to be 0.85°. After one pulse treatment (D2-48h-EP-1), the average KAM value increases to 1.04° as shown in Figure 6.9d. The D2-48h-EP-5 sample shows a significant increase in strain in the retained austenite phase (Figure 6.9g) with a KAM value of 1.3°.

The D2-48h-EP-1-LCD sample exhibits an increased KAM value of 1.16° in both the bainite and retained austenite phases, as shown in Figure 6.9f and h, respectively. The higher strain

value in the D2-48h-EP-1-LCD compared to the D2-48h-EP-1 sample is attributed to the high temperature rise in the latter case and higher athermal effect.

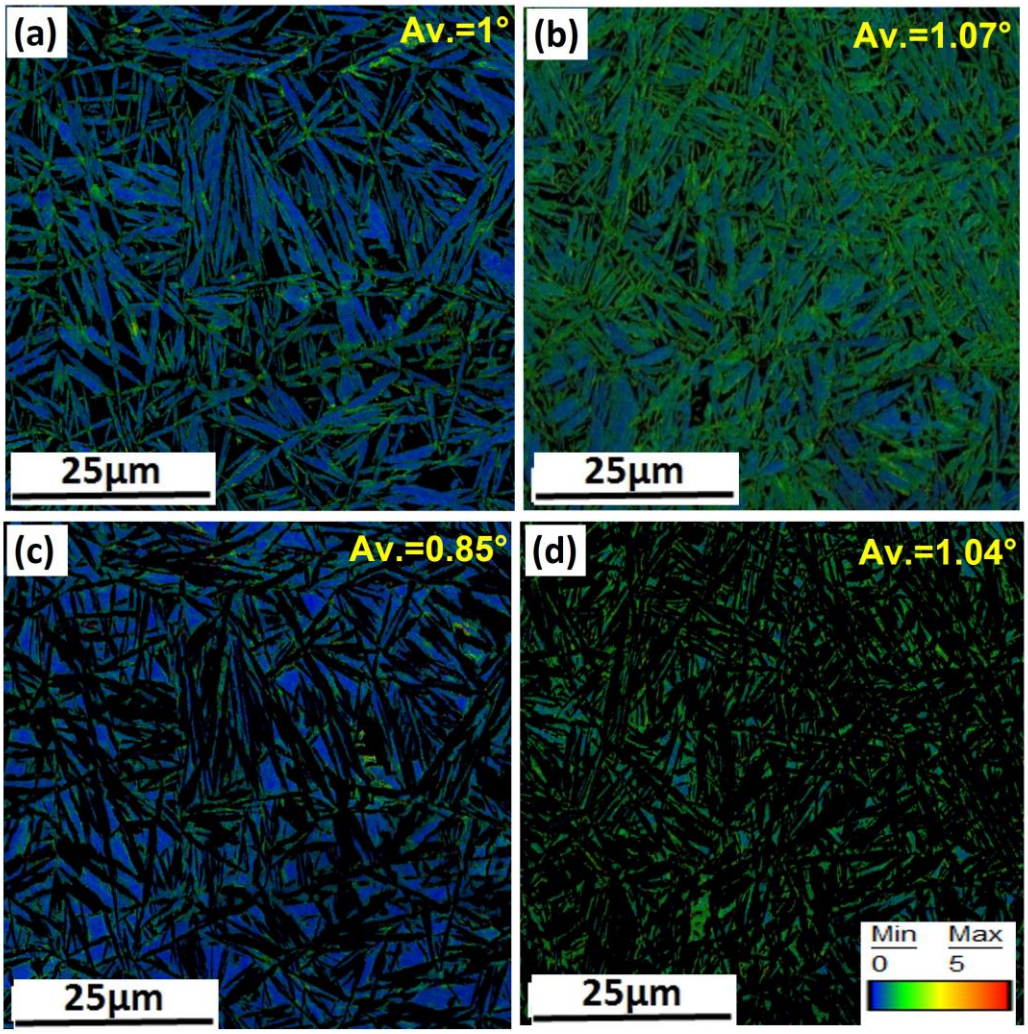

Figure 6.9. *KAM maps of bainite (a) D2-48h, (b) D2-48h-EP-1 and of retained austenite (c) D2-48h (d) D2-48h-EP-1.*

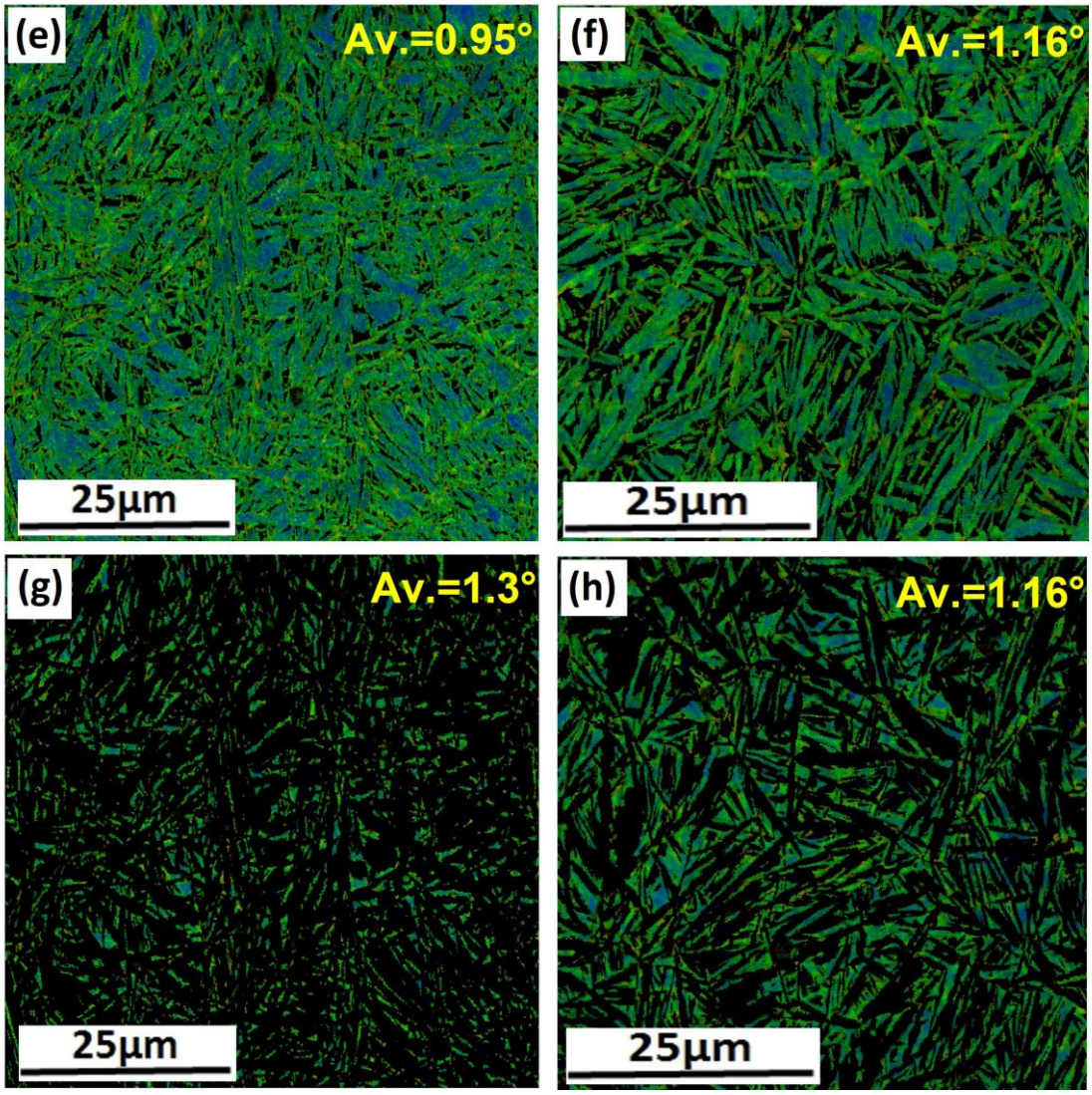

Figure 6.9 (continue…). *KAM maps of bainite (e) D2-48h-EP-5, (f) D2-48h-EP-1-LCD and of retained austenite (g) D2-48h-EP-5, (h) D2-48h-EP-1-LCD.*

The fraction of variant pairing relative to V1 is shown in Figure 6.10a-d for the D2-48h, D2-48h-EP-1, D2-48h-EP-5, and D2-48h-EP-1-LCD samples, respectively. In the D2-48h sample, the variant pair V1-V6 is the most dominant among all the pairs. After one pulse treatment (D2-48h-EP-1), the fraction of V1-V6 pair decreases, while the V1-V2 variant pair increases slightly, indicating the formation of some martensite along with bainite. In the D2-48h-EP-5 sample, the V1-V6 pairing again increases with a slight decrease in the V1-V2 variant pair. However, in the case of the D2-48h-EP-1-LCD sample, the V1-V16 pair increases slightly, but the V1-V6 pair remains dominant.

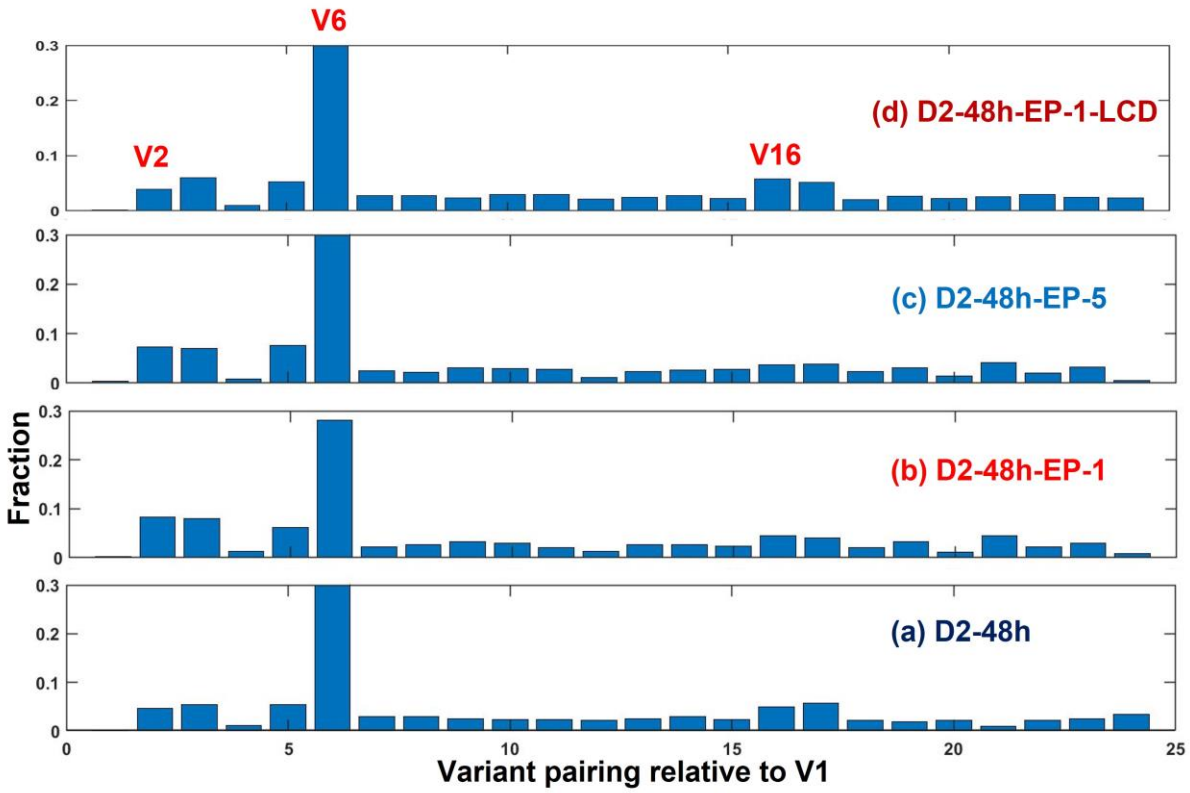

Figure 6.10. *Variant pairing with respect to V1 for (a) D2-48h (b) D2-48h-EP-1, (c) D2-48h-EP-5 and (d) D2-48h-EP-1-LCD.*

The Instrumented hardness curve at a maximum force of 5000 mN is depicted in Figure 6.11. The Vickers hardness value of the D2-48h sample is measured to be 585±23 VHN. After the first pulse treatment (D2-48h-EP-1), the hardness increases to 593±13 VHN. However, on repeated pulsing for five times (D2-48h-EP-5), the hardness value decreases again to 584±10 VHN. Notably, the D2-48h-EP-1-LCD sample shows a significant decrease in hardness value compared to the D2-48h sample (Table 6.2).

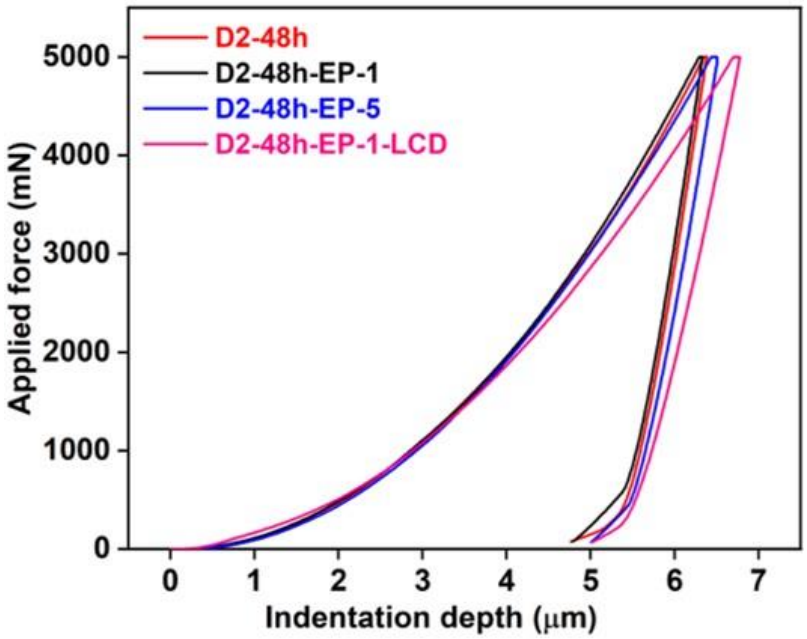

Figure 6.11. *Applied force vs. indentation depth plot*

Regarding the elastic modulus, the D2-48h sample exhibits a slight decrease after the first pulse (D2-48h-EP-1) from 198±4 GPa to 194±2 GPa. After five pulses (D2-48h-EP-5), and in the case of D2-48h-EP-1-LCD samples, the elastic modulus value is significantly decreased to 177±1 GPa and 142±2 GPa, respectively (Table 6.2).

Table 6.2. Results of instrumented hardness testing

Sample	Instrumented Hardness (HV)	Instrumented elastic modulus (GPa)
D2-48h	585±23	198±4
D2-48h-EP-1	593±13	194±2
D2-48h-EP-5	584 ±10	177±1
D2-48h-EP-1-LCD	535±9	142±2

6.3. Discussion

Electropulsing is known to have two main factors that accelerate phase transformation and bring about microstructural changes in the material. One factor is the thermal effect, such as Joule heating, which involves the conversion of electrical energy into

heat during electropulsing. The other factor is the athermal effect, which is associated with the interaction of high-velocity electrons with atoms in the material. Both of these factors play crucial roles in influencing the material's behavior during electropulsing. The subsequent sections will individually discuss these factors in detail.

6.3.1 Thermal effect of electropulsing

During EP, the temperature experiences a substantial rise of approximately 1200 °C, as previously calculated. This high temperature is rapidly cooled through radiation and convection at higher temperatures, while at lower temperatures, it is cooled by conduction aided by the presence of copper electrodes.

The equilibrium austenite start temperature of the D2-48h sample is determined to be 700 °C based on the phase stability diagram generated using Thermo-Calc software (Figure 6.12a). Despite the high temperature reached during EP, no additional austenite formation is observed in the samples. This is likely due to the short time period of the EP treatment that prevent further austenite transformation. Instead, the TEM BF images in Figure 6.4b-e clearly show the decomposition of austenite into carbide, bainite, and martensite, indicating a phase transformation rather than additional austenite formation.

Cementite precipitation is found to extend in the temperature range of about 850°C to 700°C, as indicated by the phase stability diagram. The presence of silicon in the cementite phase is believed to impede the kinetics of carbide precipitation [66]. Thus, diffusion of silicon out from the solution is necessary for carbide precipitation. The diffusion distances (L) of both silicon and carbon are calculated using Equation 6.1 [93].

$$L \approx \sqrt{Dt} \qquad (6.1)$$

Where D is the diffusion coefficient, and t is the time of holding at the temperature. The diffusion coefficient of C and Si are determined separately for BCC (D^{BCC}) and FCC (D^{FCC}) phases using Thermo-Calc software and the results are shown in Table 6.3. Considering the rapid cooling process after reaching the maximum temperature of 1200°C, it is expected that the cementite region can be traversed within 10 seconds. Therefore, for the calculation, a maximum time of 10 seconds at 750°C is considered. Using this information and the calculated diffusion coefficients, the diffusion distances for C and Si atoms in both FCC (L_{FCC}) and BCC (L_{BCC}) phases are computed and presented in Table 6.3.

Table 6.3. Diffusion coefficient and length of atomic movement.

Element	D^{FCC} (m^2/s)	D^{BCC} (m^2/s)	L_{FCC} (nm)	L_{BCC} (nm)
C	3.8 x 10^{-10}	2.5 x 10^{-9}	3.8	25
Si	4x 10^{-14}	7.4 x 10^{-13}	4x 10^{-4}	7.4 x 10^{-3}

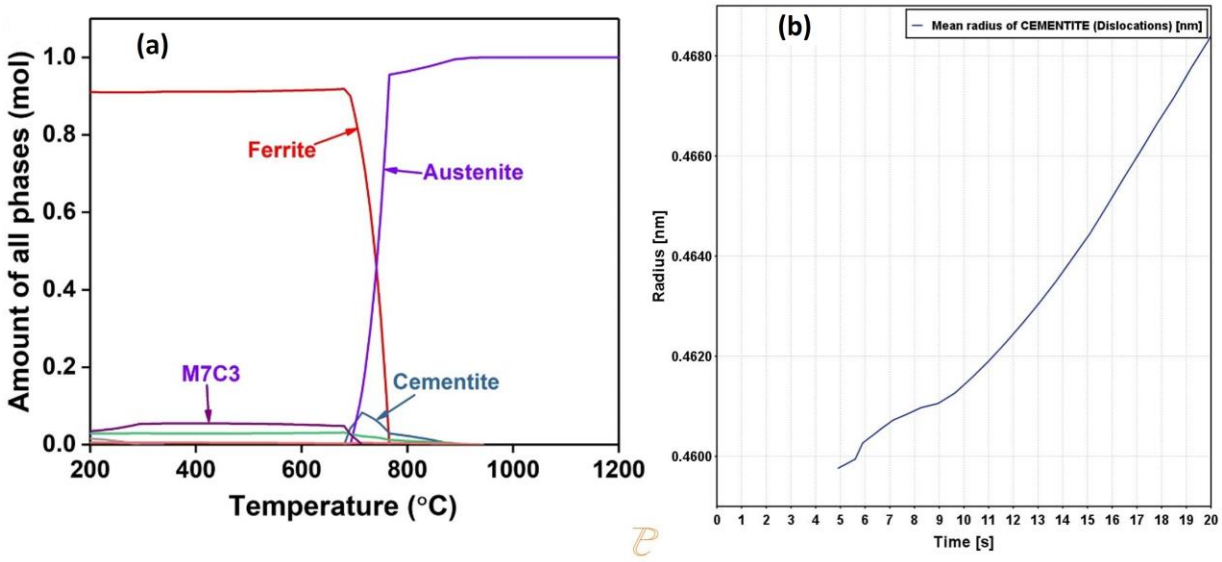

Figure 6.12. *(a) Stability of phases as a function of temperature and (b) Mean radius of cementite calculated using TC-PRISMA.*

The calculation reveals that carbon can diffuse over distances greater than the atomic distance of iron in both the FCC and BCC phases. Similarly, the movement of silicon in the BCC phase is greater than in the FCC phase, but the diffusion distance is still much less than the atomic distance of the Fe atom (0.286 nm).

Based on these results, it can be inferred that carbides are primarily forming due to the movement of carbon atoms rather than silicon atoms. The ability of carbon to diffuse over relatively long distances compared to silicon in the BCC and FCC phases suggests that carbon plays a dominant role in the precipitation of carbides in the material.

In order to investigate the possibility of cementite precipitation in the D2-48h sample through heating alone, simulations are conducted using the TC-PRISMA module (Steels and Fe-alloys (TCFE8, MOBFE3) package) within the Thermo-Calc software, as depicted in Figure 6.12b. In this simulation, the matrix phase is considered as austenite with an initial carbon content of 1.15 mass%, and cementite precipitation is calculated at 750 °C for 20 seconds. Notably, the bainite phase is not included in the calculation since it already contains some minor quantity of carbides. Additionally, simulations for other precipitates, like M_7C_3, show no signs of precipitation except for cementite.

The mean radius of cementite precipitation from austenite is calculated to be 0.468 nm at 750 °C for a 20-second holding time. However, this value is significantly smaller than the observed radius of cementite (28 nm) in TEM micrographs (Figure 6.4c). This discrepancy clearly indicates that the observed precipitate size cannot be solely attributed to the thermal effect. Other factors, such as athermal effects, are likely to contribute to the observed precipitate size and distribution.

In the lower current density sample (D2-48h-EP-1-LCD), the temperature rise is relatively low at 470 °C, which is not sufficient to induce the precipitation of any fresh cementite. The

observed carbides in the bainite phase of the austempered sample (D2-48h) exhibit slight growth after undergoing electropulsing at the lower current density (D2-48h-EP-1-LCD). This growth could be a result of the effect of electropulsing treatment at the lower current density on the existing carbides rather than the formation of fresh cementite precipitates due to the lower temperature rise.

6.3.2 Athermal effect of electropulsing

The high-speed electrons exert a force on atoms during EP to cause drifting. Generally, electrons that are ionised move from cathode to anode creates vacancies [143]. In presence of vacancies rate of diffusion is accelerated. The atomic diffusion flux (*J*) in presence of pulse current is already given by Equation 3.4 [143,145].

$$J = \frac{2Nez^{*}D\rho_{r}If\Delta t}{KT}$$

From Arrhenius equation, it is clear that diffusion coefficient is related to temperature as given in Equation 6.2 [93].

$$D = D_0 \exp(-Q/RT) \qquad (6.2)$$

Here *Q* is the activation energy and *R* is universal gas constant. From equation 3.4 and 6.2, it is clear that temperature has contribution in atomic diffusion both in thermal and athermal equations of EP.

6.3.3 Carbide precipitation and dissolution

The phase stability diagram (Figure 6.12a) indicates that the formation of M_7C_3 and cementite, along with ferrite and austenite phases, is thermodynamically feasible. However, simulations using TC-PRISMA show no driving force available for M_7C_3 precipitation in the austenite phase. Therefore, the observed carbides are mainly identified as cementite or some

intermediate iron-based carbides like epsilon carbide. In the bainite phase, there can be a driving force for M_7C_3 precipitation as carbon is already present in the form of fine carbides, clusters, and in a supersaturated condition. Silicon (Si) is believed to come out from cementite for its precipitation, but the maximum distance a Si atom can move by the thermal effect of EP is calculated to be less than an atomic distance. As a result, cementite precipitation by the movement of Si is ruled out. An alternative way of carbide precipitation is through the para-equilibrium method, where carbon moves towards other clusters to form carbides rather than the movement of Si. This evidence has been provided by Ghosh and Olson [68].

TEM micrographs of the D2-48h-EP-1 sample reveal extremely tiny spherical carbides (Figure 6.5c) and elongated carbides (Figure 6.4c). The fine precipitates essentially form during the cooling stage of the sample after reaching the maximum temperature of 1200 °C due to Joule heating from EP. However, the formation of elongated carbides is attributed to the combined effects of temperature and athermal effects, such as high-velocity electric current, as discussed earlier. Additionally, the already present fine carbides and clusters in the bainite phase of the austempered sample are observed to grow to relatively larger sizes, which are not predicted in the simulation.

In the case of the low current density sample (D2-48h-EP-1-LCD), both the temperature and current density are lower compared to the high current density samples, which results in the diminished growth of precipitates compared to the latter case. There is no precipitation in the RA phase due to the low current density and time period. Although there are reports that current densities exceeding 10^3 A/mm^2 can effectively migrate atoms [42,231], no carbide precipitation is observed as the temperature effect is less pronounced here. Thus, a combination of thermal and athermal effects is required to induce any such changes during electropulsing.

Repeated EP lowers the resistivity of the material by either transforming to a higher conducting phase or by aligning the phases in a way that decreases resistivity [179,232]. The electrical resistivity, measured using a four-probe technique with a micro-ohm meter, shows a decreasing trend with an increasing number of pulses. The initial austempered sample had an electrical resistivity value of 9.2 x 10-7 Ωm, which decreased to 8.1 x 10-7 Ωm and 7.5 x 10-7 Ωm after one pulse (D2-48h-EP-1) and five pulses, respectively. The electrical resistivity decreases in the order of cementite, austenite, martensite, and bainite [119].

After one pulse, carbides are formed from supersaturated bainite and austenite due to the combined effect of the current pulse and temperature. The formation of carbides leads to a depletion of carbon in the matrix, as confirmed by the estimated carbon content in RA, which is 0.9 mass%. Subsequent pulses result in the dissolution of carbides formed after the first pulse (D2-48h-EP-1), leading to an increase in carbon content in RA (0.99 mass %). This dissolution is evident from the DF images of TEM (Figure 6.6c), where complete dissolution in the RA and partial dissolution in the bainite phase is observed. Earlier works [233] also confirm that EP can accelerate the dissolution of carbides due to the energy difference between the particle and matrix.

6.3.4 Electropulsing assisted bainite and martensite formation

The effect of EP on the bainite and RA can be divided into two stages. The first stage occurs during pulsing, where most athermal changes, such as accelerated movement of atoms, take place and the second stage is related to Joule heating. A recent study on medium Mn steel reveals the transformation of coarse austenite to martensite due to the athermal effect of EP [234]. The underlying mechanism is believed to be the weakening of bond strength and elastic modulus due to the passage of a high-density current pulse [235]. In the present study, due to pulsing, the elastic modulus is observed to decrease, as evidenced by instrumented hardness

testing, resulting in the formation of diffusionless products like bainite and martensite. As a consequence of prior carbide formation due to both thermal and athermal influences, the RA experiences carbon depletion, causing an increase in the Ms temperature to 55°C. Consequently, the BRA exhibits twinned martensite, as shown in Figure 6.5a-c.

The fundamental difference between bainitic and martensitic transformations lies in the diffusion of carbon during the nucleation stage. In the case of bainitic transformation, carbon diffusion is necessary to provide the required driving force for the process to occur. In contrast, martensitic transformation is entirely diffusionless for carbon and other substitutional elements [119]. The evidences supporting the formation of bainite during EP is discussed as follows.

Thermodynamically, a phase with higher conductivity is expected to form during electropulsing, as discussed in Section 1.6.1 of chapter 1. The RA phase, being higher in resistance, should transform into a more conductive phase, such as ferrite, bainite, or martensite [75] during the passage of the electric current pulse. However, the rapid heating and cooling cycles during EP restrict the formation of ferrite, which is also not observed in the TEM BF images. Therefore, bainite, being more conductive compared to martensite, is most likely to form during pulsing. Kinetically, EP also promotes bainite formation by accelerating carbon diffusion, which is required during the nucleation stage to provide the necessary driving force for the transformation to occur.

XRD analysis provides additional evidence of bainite formation during EP. If we assume that only martensite is formed during pulsing, it would need to accommodate all the carbon present in the RA (0.9 mass%). This much carbon in the martensite phase would lead to the appearance of additional tetragonal peaks near the original positions of the reflection or significant asymmetry in the XRD pattern. Furthermore, XRD peak broadening or shifting towards a lower

Bragg angle would occur due to the presence of high carbon in the martensite. However, the experimental XRD results after EP show no sign of asymmetry and the peaks are shifted towards a higher angle side compared to the initial non-pulsed sample. This pattern suggests that the formation of martensite is not significant compared to bainite.

From the calculations of dislocation density in the RA phase using XRD and qualitative information from the KAM map, it has been observed that the dislocation density increases after EP. The generation of dislocations occurs during the bainitic transformation [130] as well as martensitic trsnsformation at higher temperatures [236]. However, as the martensite start temperature is about 55°C, there is less chance of dislocation generation at lower temperature. The increase in dislocation density further supports the occurrence of bainitic transformation during the EP process.

Furthermore, bainite formation from the RA can be indirectly supported by the variant pairing analysis, as depicted in Figure 6.10. In the case of high carbon martensite, the dominating variant pair is V1-V2, along with other variants [88], However, in the present study of electropulsing, V1-V6 is the dominant pair in all cases, indicating the prevalence of bainitic transformation.

The combination of several factors contributes to the instant bainite formation and the formation and dissolution of carbides during electropulsing. Firstly, the decrease in elastic modulus, along with the thermodynamic effect favoring the formation of a higher conductive phase, plays a crucial role. Secondly, the kinetic effect of accelerated carbon diffusion is another significant factor driving bainite formation. Together, these factors promote rapid changes in the microstructure during EP, resulting in the observed formation of bainite and other phases

6.4. Conclusions

The main findings from passing a high-density electric current pulse through nanostructured bainitic steel with a significant amount of retained austenite can be summarized as follows:

- Electropulsing of retained austenite accelerates bainitic transformation. The rapid migration of carbon to generate a potential nucleation site and the lowering in elastic modulus in the presence of current pulse enable the blocky RA to transform into bainite.
- Kinetics of bainitic transformation is accelerated with increasing current density.
- Electropulsing can induce martensitic transformation along with bainitic transformation.
- The initial electric pulse can induce carbide precipitation in both the retained austenite and in the bainite/martensite phases. However, repeated pulses can redissolve carbides in bainite/martensite and austenite. After five pulses carbide precipitates are completely dissolved in austenite of higher solubility, while they are decreased in bainite.
- Estimating the growth kinetics of precipitates indicates that the observed sizes cannot be solely explained by thermal effects during heating and cooling processes. The kinetics of carbide precipitation are accelerated by the enhanced mobility resulting from the athermal effect of electropulsing, rather than relying solely on thermal effects.
- Carbide precipitation in blocky retained austenite leads to a decrease in chemical stability. As a result, the carbon-depleted austenite also undergoes partial transformation into martensite during cooling to room temperature.
- Hardness of austempered steel increases at initial pass of electropulsing due to additional transformation. On further pulsing the material is softened due to dissolution of carbides and partial recovery of defects, though additional bainite and martensite are formed from retained austenite.